ELSEVIER

Journal of Nuclear Materials 318 (2003) 249–259

journal of nuclear materials

www.elsevier.com/locate/jnucmat

Microstructural analysis of 9% Cr martensitic steels containing 0.5 at.% helium

J. Henry [a,*], M.-H. Mathon [b], P. Jung [c]

[a] CEA Saclay, SRMA, F-91 191 Gif-sur-Yvette cedex, France
[b] LLB (CEA-CNRS), CEA Saclay, F-91 191 Gif-sur-Yvette cedex, France
[c] Institut für Festkörperforschung, Forschungszentrum Jülich, D-52425 Jülich, Germany

Abstract

Microstructural examinations by transmission electron microscopy and small angle neutron scattering were performed on 100 μm thick specimens of 9Cr–1Mo (EM10) and modified 9Cr–1Mo (T91) martensitic steels homogeneously implanted with 23 MeV α particles to a concentration of 5000 appm. Two implantation temperatures were selected, 250 and 550 °C, which correspond respectively to the lower and higher bounds of the operation temperature range foreseen for the window of accelerator driven systems devoted to waste transmutation. 250 °C is also the maximum operating temperature of the European spallation source window. The TEM samples were punched out from implanted tensile specimens following testing, which revealed, as detailed in a companion paper [P. Jung et al., these Proceedings], drastic hardening and complete ductility loss for the specimens implanted at 250 °C. Helium bubbles were detected in both materials implanted at 250 and 550 °C and bubble size distributions as well as number densities were determined. Furthermore, it was found that the bubbles are at thermodynamic equilibrium. Based on the microstructural results, it is shown that the high degree of hardening of specimens implanted at 250 °C is due to the high density of tiny helium bubbles they contain. It is furthermore suggested that the brittle, intergranular fracture mode displayed by these specimens results from the combined effects of pronounced intragranular hardening and weakening of prior austenite grain boundaries due to helium.

1. Introduction

It has been known for many years that helium can have deleterious effects on the mechanical properties of steels, but up to now the He-related investigations were mainly focused on operating conditions relevant for the structural materials of fusion devices, i.e. high temperatures and moderate helium concentrations. The operating temperature range of the proton beam windows of future liquid metal spallation sources will be lower than that of the first wall of a fusion reactor. In addition, the helium generation rate will be approximately one order of magnitude higher leading to a build-up of large quantities of helium within a few months of operation. For instance the expected accumulated concentration in the European spallation source (ESS) window within 6 months is estimated to be about 0.5 at.% [2]. Due to the lack of data for such high helium concentrations, especially at low temperature, implantation experiments of 9Cr–1Mo martensitic steels, which are candidate materials for the window of ADS, were recently carried out. It was shown that the tensile properties of these steels are dramatically affected by the implantation of 5000 appm He at 250 °C, whereas the effect of the same amount of helium when implanted at 550 °C is much less pronounced. The specimens implanted at 250 °C displayed a very high degree of hardening and fracture occurred with virtually no plastic deformation in a fully brittle, predominantly intergranular mode. Additional

* Corresponding author. Tel.: +33-1 69088508; fax: +33-1 69087130.
E-mail address: jean.henry@cea.fr (J. Henry).

0022-3115/03/$ - see front matter © 2003 Elsevier Science B.V. All rights reserved.
doi:10.1016/S0022-3115(03)00118-1

implantation experiments were performed to different concentrations and at temperatures ranging from room temperature up to 550 °C. A comprehensive presentation of the tensile tests results is given in a companion paper [1]. In the present contribution, we report on the microstructural analysis of 9Cr–1Mo specimens implanted with 5000 appm He at either 250 or 550 °C, using transmission electron microscopy (TEM) and small angle neutron scattering (SANS). Based on the microstructural information obtained by these two complementary technique, the results of the tensile tests will be briefly discussed.

2. Experimental

2.1. Materials and helium implantation

Two martensitic steels were used in this study: unstabilised 9Cr–1Mo (EM10 grade) and Mod 9Cr–1Mo VNb (T91 grade) whose chemical compositions are given in Table 1. One 0.5 mm thick plate of each material was cold rolled in order to obtain sheets about 100 μm in thickness. Two types of specimens were cut by spark erosion (Fig. 1): miniature tensile specimens, with a gauge length of 12 and 2 mm width, and 'H-shaped' specimens of overall dimensions $30 \times 10 \times 0.1$ mm. The latter specimens were used for the SANS experiments and will be referred to in the following as 'SANS specimens'. The as-machined specimens were subsequently heat-treated. The details of the normalisation and tempering treatments are as follows: 15 min at 970 °C followed by 30 min at 750 °C for EM10 and 1 h at 1050 °C plus 1 h at 760 °C for T91. Prior austenite grain (PAG) size measurements showed a broad size distribution with average values of 21 μm in the case of EM10 and 14 μm for T91.

Details of helium implantation are presented in [1]. In contrast to the four tensile specimens only one SANS specimen was mounted on one holder for each implantation run. In [1] it is also described that the implantation of one helium atom produces on the average 155 atomic displacements according to calculations by the TRIM code [3,4].

2.2. TEM

Following implantation and testing of the tensile specimens, one 2 mm disc was punched out from the gauge section of each specimen and thin foils suitable for TEM examinations were prepared by jet-electropolishing. No TEM discs were punched from the SANS specimens since these are intended to be used to prepare tips for tomographic atom probe experiments. TEM observations were performed using a Philips EM430 microscope and a Jeol 2010-F microscope operating at 300 and 200 kV, respectively. Bubble and black dot sizes were determined using a semi-automatic size-measurement device. For the determination of densities, thickness measurements were performed using the convergent-beam diffraction technique [5].

2.3. Small angle neutron scattering experiments

The neutron scattering experiments were carried out at Laboratoire Léon Brillouin (CEA-CNRS), using the PAXE small angle instrument. With a neutron wavelength λ and sample to detector distance of 0.6 nm and 2 m, respectively, a range between 0.3 and 1.6 nm^{-1} for the scattering vector q was covered. Due to the small

Table 1
Compositions of the materials (in wt%)

Steel	C	Cr	Mo	V	Nb	Ni	Mn	N	P	Si
EM10	0.096	8.8	1.09	–	–	0.18	0.51	0.024	0.015	0.37
T91	0.105	8.26	0.95	0.2	0.075	0.13	0.38	0.0055	0.009	0.43

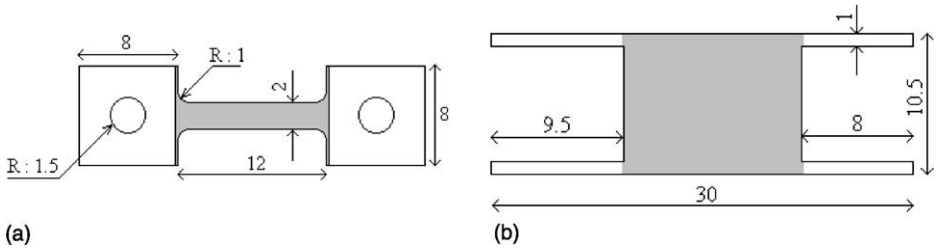

Fig. 1. Schematic showing (a) the dimensions of the miniature tensile specimens and (b) the dimensions of the 'SANS' specimens. Numbers give dimensions in mm. For each type of specimen the zone implanted with helium is shaded.

volume of material involved in the scattering experiments (about 3.5 mm^3), long measurements times (8–10 h) were necessary to obtain sufficiently small statistical errors. Measurements were performed under saturating magnetic field ($H = 2T$), perpendicular to the incident neutron beam direction so as to separate magnetic and nuclear scattering cross-sections. The intensity scattered by an unimplanted reference specimen (either EM10 or T91) was substracted from the intensities scattered by the implanted samples in order to eliminate the incoherent scattering and the contributions from inhomogeneities such as free surfaces, grain boundaries, carbides etc. Background correction and calibration were performed as described in [6].

3. Results

3.1. TEM

3.1.1. Specimens implanted at 550 °C

As expected, TEM examinations showed the presence of helium bubbles in the specimens implanted at 550 °C. The bubbles were imaged using the phase contrast technique [7]. In under-focus imaging conditions, bubbles appear surrounded by dark fringes which allow to determine their sizes. In both materials, the bubble microstructure was found to be very similar. The bubbles are heterogeneously distributed: as shown on Fig. 2, they are located on PAG boundaries, on lath and subgrain boundaries as well as on the dislocations inside the laths and on the carbide-matrix interfaces. The bubbles are either spherical or facetted and some are very elongated. The bubble sizes were measured on high-magnification micrographs as shown on Fig. 3. In the case of a facetted bubble, the given size corresponds to the radius of a spherical bubble of equal projected surface. More than 2000 bubbles for each specimen were involved in the size measurements. Size-histograms are reported in Fig. 4(a) and (b) for EM10 and T91, respectively. In order to determine the bubble densities, about 3000 bubbles were counted on micrographs corresponding to different PAGs of each TEM thin-foil. The results of the bubble analysis are given in Table 2. It must be mentioned that the bubble densities were found to vary significantly (up to a factor of three) depending on the chosen region of each specimen.

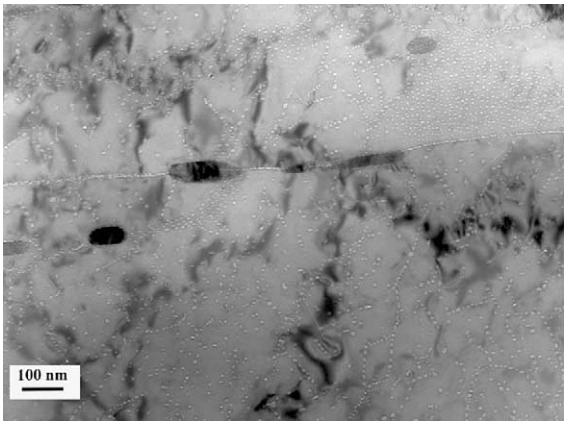

Fig. 2. TEM micrograph showing the bubble microstructure in EM10 implanted with 0.5 at.% He at 550 °C. Under-focus imaging conditions ($\delta f = -1000$ nm).

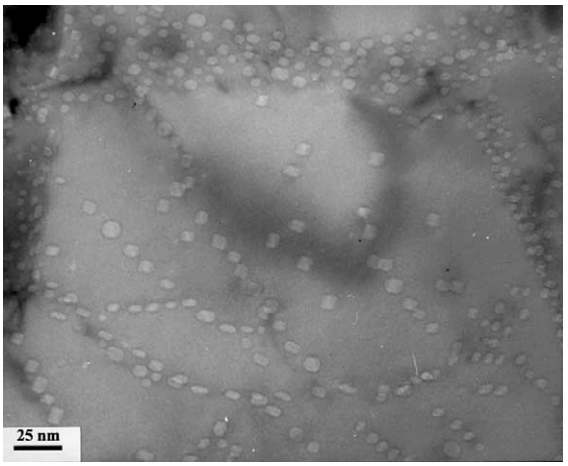

Fig. 3. TEM high magnification micrograph showing bubbles in EM10 implanted at 550 °C with 0.5 at.% He.

3.1.2. Specimens implanted at 250 °C

In both samples implanted at 250 °C, a black dot microstructure was revealed by TEM, as illustrated on Fig. 5. This microstructure results from the implantation-induced damage evaluated to be about 0.8 dpa according to TRIM calculations (see Section 2.1). The black dot sizes and densities were found to be identical for both materials within experimental uncertainties. The measured values of mean black dot diameters are 3.7 and 3.5 nm and the corresponding black dot number densities 3.5×10^{22} and 3×10^{22} m^{-3} for EM10 and T91, respectively. Helium bubbles could not be detected by TEM.

3.2. SANS

The scattering cross-sections of the implanted specimens are given in Fig. 6. The intensity scattered by the samples implanted at 550 °C is obviously due to the helium bubbles detected by TEM. No other implantation induced microstructural features such as black dots/dislocation loops nor any modification of the carbide microstructure were revealed by the TEM analysis. Furthermore, it must be mentioned that scattering spectra were measured for one EM10 and one T91

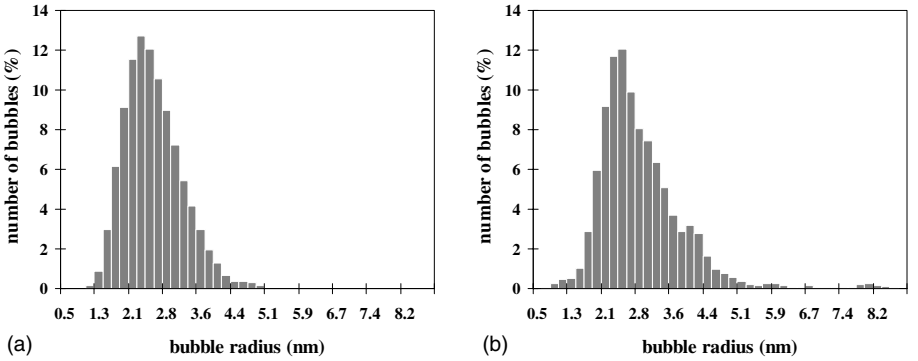

Fig. 4. (a) Bubble size-distribution in EM10 implanted at 550 °C with 0.5 at.% He. (b) Bubble size-distribution in T91 implanted at 550 °C with 0.5 at.% He.

Table 2
Results of the TEM analysis of the bubble microstructures in EM10 and T91 implanted to 0.5 at.% He at 550 °C

	R_m (nm)	ΔR (nm)	N_b (m^{-3})
EM10 implanted at 550 °C	2.5	0.6	4.2×10^{22}
T91 implanted at 550 °C	2.85	0.9	3.0×10^{22}

R_m is the mean radius, ΔR is the standard deviation of the size distribution and N_b the bubble number density.

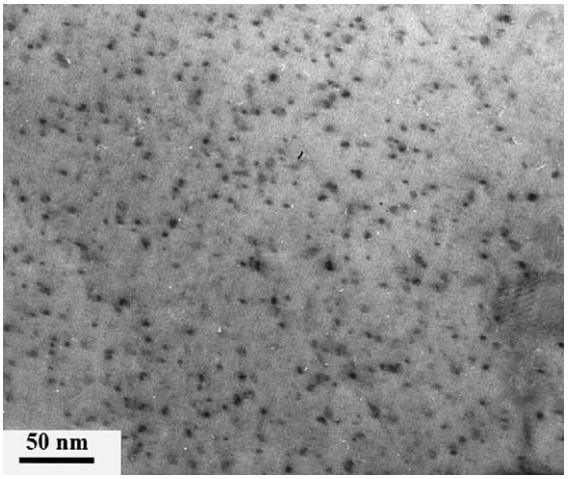

Fig. 5. Bright field TEM micrograph showing small defect clusters, $g = 110$, $s > 0$. EM10 implanted with 0.5 at.% He at 250 °C.

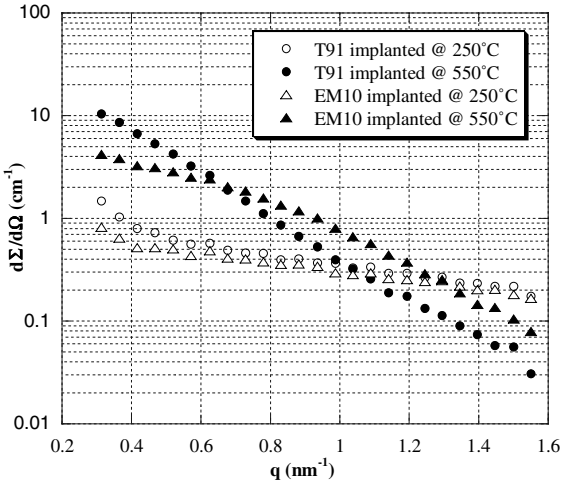

Fig. 6. Implantation-induced scattering cross-sections measured perpendicularly to the applied magnetic field.

specimen following annealing at 550 °C for 70 h, which corresponds to the implantation time. Virtually no variation of the scattering intensities was observed between the annealed and the reference samples, showing that the microstructure did not evolve after 70 h at 550 °C.

With respect to the implantation-induced scattered intensities for the samples implanted at 250 °C, one has to assess the contribution to the total scattering cross-section of the high density of small defect clusters, which are probably small dislocation loops, detected by TEM. Based on the theory of small angle scattering of small dislocation loops [8], it is shown in Appendix A that this contribution is many orders of magnitude smaller than the measured intensity. Therefore, although they were not detected by TEM, it must be concluded that the scattered intensity is mainly due to helium bubbles.

In terms of cross-section, the intensity scattered by helium bubbles can be written as

$$\mathrm{d}\Sigma/\mathrm{d}\Omega = \sum_{b=1}^{N_b} (\Delta\rho_{nuc}^2 + \Delta\rho_{mag}^2 \sin^2\alpha) V_b^2 F_b^2(q), \quad (1)$$

where α is the angle between the magnetisation of the sample and the scattering vector q. N_b is the number of bubbles contained in the sample and F_b the form factor of a bubble. $\Delta\rho_{nuc}$ and $\Delta\rho_{mag}$ are the nuclear and magnetic contrast, respectively, which depend in the following way on the coherent magnetic length in the matrix b_{mag}^m, and on b_{nuc}^m and b_{nuc}^b the coherent nuclear scattering lengths in matrix and in the helium bubbles, respectively.

$$\Delta\rho_{nuc} = b_{nuc}^m/\Omega_m - b_{nuc}^b/\Omega_{He}, \quad (2)$$

$$\Delta\rho_{mag} = b_{mag}^m/\Omega_m, \quad (3)$$

Ω_m and Ω_{He} are the atomic volumes of the matrix and of the helium contained in a bubble, respectively. Ω_{He} is directly related to the helium pressure inside a bubble, which is expected to depend on the bubble size, as confirmed experimentally in nickel, for instance [9]. b_{nuc}^m was calculated from the known coherent scattering lengths of the different elements in solid solution in the matrix. Due to the small difference between the values obtained for EM10 and T91, which is negligible compared to the uncertainties on the experimental data for the individual elements, a unique value was used for the analysis of the scattering spectra. b_{mag}^m was determined as follows:

$$b_{mag}^m = (\gamma e/2m_0c^2) f(q) \mu_m, \quad (4)$$

where γ is the magnetic moment of the neutron, e and m_0 the electron charge and mass, respectively. $f(q)$ is the atomic form factor, which is equal to 1 at small angles and μ_m the mean magnetic moment per matrix atom, which was calculated as follows [22]:

$$\mu_m = M_0 - M_1 C_{Cr}, \quad (5)$$

where C_{Cr} is the chromium concentration in the matrix. M_0 and M_1 are equal to 2.20 and 2.39 μ_B per atom, respectively, where μ_B is the Bohr magneton.

Since all magnetic moments are aligned parallel to the applied magnetic field, one can extract the maximum magnetic scattered intensity $(\mathrm{d}\Sigma/\mathrm{d}\Omega)_{mag}$ from $(\mathrm{d}\Sigma/\mathrm{d}\Omega)_{\parallel}$ and $(\mathrm{d}\Sigma/\mathrm{d}\Omega)_{\perp}$, which are the intensities measured respectively parallel and perpendicular to the external magnetic field:

$$(\mathrm{d}\Sigma/\mathrm{d}\Omega)_{mag} = (\mathrm{d}\Sigma/\mathrm{d}\Omega)_{\perp} - (\mathrm{d}\Sigma/\mathrm{d}\Omega)_{\parallel} = \sum_{b=1}^{N_b} \Delta\rho_{mag}^2 V_b^2 F_b^2(q). \quad (6)$$

In this way, one eliminates the nuclear contrast, which depends on an unknown quantity, the helium density. The contrast is no longer size-dependent and Eq. (6) can be written as

$$\frac{1}{V_s}(\mathrm{d}\Sigma/\mathrm{d}\Omega)_{mag} = f_b \Delta\rho_{mag}^2 \left(\int_0^\infty h(R) V^2(R) F^2(q,R)\,\mathrm{d}R \right) \Big/ \left(\int_0^\infty h(R) V(R) F(q,R)\,\mathrm{d}R \right) \quad (7)$$

where f_b is the bubble volume fraction, $h(R)$ the size distribution and V_s the volume of the sample. Here we have assumed for simplicity that all helium bubbles are spherical. We have seen in the TEM section (Section 3.1.2) that while a significant fraction of the bubbles are spherical, numerous faceted bubbles are also found. Since the majority of these are roughly cubic in shape, it is not unreasonable to use for all bubbles the structure factor for spheres. We have furthermore assumed that the bubble size distribution can be described by a Gaussian distribution.

With these assumptions, it is possible to determine the mean bubble size R_m, the width of the size distribution, characterised by the half-width at half maximum ΔR, and the volume fraction f_b. These three adjustable parameters are calculated by a fit of the experimental data using Eq. (7). The obtained values are given in Table 3, together with the corresponding bubble number densities N_b. One should finally point out that in the fitting procedure used in the present work, interference effects between particles were neglected, which is generally justified when the volume fractions of scattering objects are low, as is the case here. However, since TEM revealed that the bubble distributions were highly

Table 3
Results of the SANS analysis of the bubble microstructures in EM10 and T91 implanted to 0.5 at.% He at 250 °C and 550 °C

	R_m (nm)	ΔR (nm)	f_b (%)	N_b (m^{-3})
EM10 implanted at 250 °C	1.2	0.38	0.79	8.5×10^{23}
T91 implanted at 250 °C	1.15	0.35	0.95	1.17×10^{24}
EM10 implanted at 550 °C	2.4	0.4	0.96	1.5×10^{23}
T91 implanted at 550 °C	2.8	1	0.83	6.5×10^{22}

R_m is the mean radius, ΔR is the half-width at half maximum, f_b the bubble volume fraction and N_b the bubble number density.

heterogeneous in the samples implanted at 550 °C, the SANS data were also fitted using a hard sphere-type model [23], which takes into account possible interference effects. The obtained results were very close to those given in Table 3.

The comparison of the parameters characterising the bubble populations in EM10 and T91 implanted at 550 °C (Tables 2 and 3) shows that there are some discrepancies between the results given by TEM and SANS, especially as regards the bubble number densities. Different points have to be mentioned which might explain, at least to some extent, the observed differences. First, it is estimated that the error induced by the preliminary SANS data treatment (background correction and calibration) on the value of the volume fraction is about 15%. There is also an uncertainty on the magnetic contrast, due to the fact that value for the magnetic moment was taken equal to that of pure iron. However, although the error on the magnetic moment is not precisely known, it is thought to be small. On the other hand, the error on the densities measured by TEM is at least equal to 10%, due mainly to the uncertainty on the thickness measurements.

In addition, TEM and SANS were not carried out on the same specimens, as mentioned in Section 2.1. Temperature measurements by pyrometry showed that there was a temperature gradient across the surface of the SANS specimens. Due to their small width, the tensile specimens were not affected by the same problem. For the SANS samples implanted at a nominal temperature of 550 °C, the temperature in the centre of the specimens was close to this value, whereas the temperature in the outer part was lower, especially in the case of the EM10 specimen. In the region involved in the SANS measurements (a disc 8 mm in diameter), the lowest temperature was approximately 360 and 420 °C for EM10 and T91, respectively. As a result, the bubble density in the cooler region of the specimen is expected to be higher than in the central part. This contributes to the higher density values obtained by the SANS analysis compared to the TEM results.

In addition to the size distributions and bubble densities, the experimental data can also provide informations concerning the helium density, via the so-called A ratio, defined as

$$A(q) = \frac{(\mathrm{d}\Sigma/\mathrm{d}\Omega)_{\perp}}{(\mathrm{d}\Sigma/\mathrm{d}\Omega)_{\parallel}}. \tag{8}$$

For a population of bubbles of equal radius r, the A ratio becomes independent of the scattering vector and takes the very simple expression:

$$A = \frac{\Delta\rho_{\mathrm{nuc}}^2 + \Delta\rho_{\mathrm{mag}}^2}{\Delta\rho_{\mathrm{nuc}}^2} = 1 + \left(\frac{b_{\mathrm{mag}}^{\mathrm{m}}/\Omega_{\mathrm{m}}}{b_{\mathrm{nuc}}^{\mathrm{m}}/\Omega_{\mathrm{m}} - b^{\mathrm{He}}/\Omega_{\mathrm{He}}(r)} \right)^2. \tag{9}$$

The experimental values of $A(q)$ are plotted in Figs. 7 and 8 for T91 and EM10, respectively. No obvious q-dependence can be detected from the experimental data. The mean values of A are given in Table 4.

In Fig. 9, we have plotted the variation of the helium density as a function of the bubble radius r, using the Trinkaus EOS for helium [10] and assuming that the bubbles are in thermodynamic equilibrium, i.e. that their internal pressure is balanced by the surface tension $2\gamma/r$. The dependence of A on the bubble size, obtained using Eq. (9) and the helium density values at thermodynamic equilibrium, is also plotted for the two implantation temperatures. The experimental values of the mean A

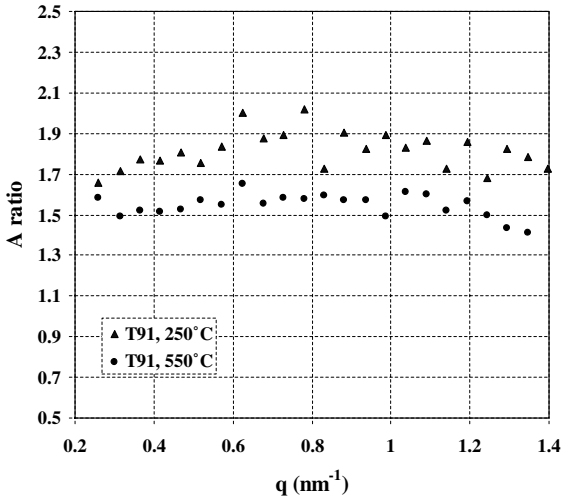

Fig. 7. A ratio as a function of the scattering vector q for T91 implanted with 0.5 at.% helium at 250 and 550 °C.

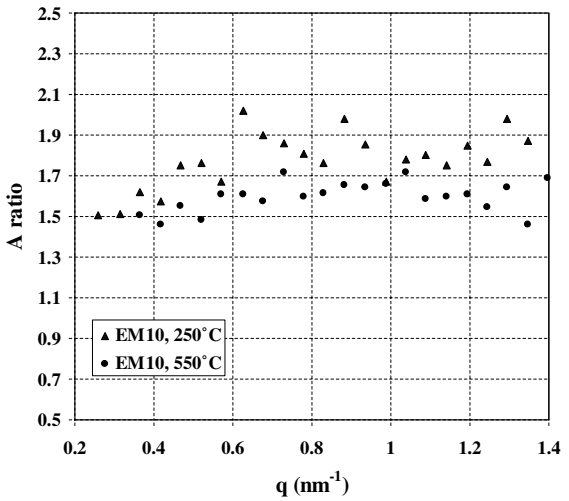

Fig. 8. A ratio as a function of the scattering vector q for EM10 implanted with 0.5 at.% helium at 250 and 550 °C.

Table 4
Mean values of the A ratio

	A
EM10 implanted at 250 °C	1.8 ± 0.15
T91 implanted at 250 °C	1.8 ± 0.15
EM10 implanted at 550 °C	1.6 ± 0.10
T91 implanted at 550 °C	1.5 ± 0.18

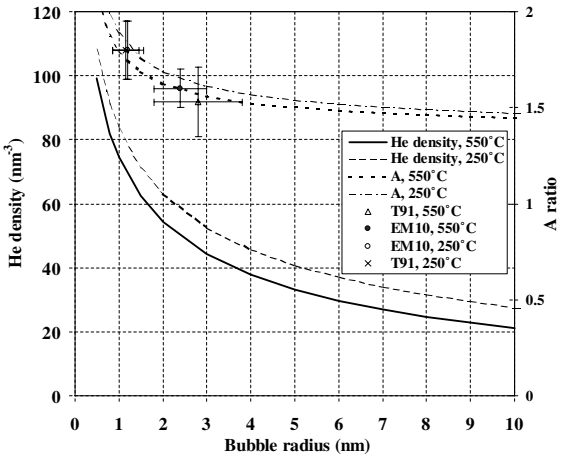

Fig. 9. Helium density and A ratio as a function of the bubble radius. The curves showing the helium densities at 250 and 550 °C where calculated using the Trinkaus EOS for helium [10] and a surface energy $\gamma = 1.8$ Nm^{-1} and assuming that the bubbles are in thermodynamic equilibrium. The curves showing the evolution of A ratio vs. bubble radius were obtained via Eq. (9) and using the calculated helium densities. The symbols correspond to the experimental values of A as given in Table 4. The horizontal bars indicate the HWHM of the bubble size distributions (cf. Table 3) and the vertical bars correspond to the scatter of A over the investigated q-range (cf. Table 4).

ratio are plotted as well. From Fig. 9, it can be concluded that the bubbles are close to thermodynamic equilibrium. This conclusion is different from that of Qiang-Li et al. [9] concerning the densities in bubbles formed in helium-implanted nickel. They found that the pressure inside the bubbles was above that expected for bubbles at thermodynamic equilibrium. However, these bubbles were obtained by isochronal annealing steps at 1173 K following implantation at room temperature. In this case, the overpressure is thought to result from the inability of the dislocations to supply the required amount of vacancies for relaxation to occur [9]. In the present work, the bubbles are formed during the implantation process, which results in a continuous supply of vacancies.

Finally, it must be mentioned that a T91sample irradiated with fission neutrons at 325 °C to 0.8 dpa was recently analysed by SANS [24]. The scattered intensity is thought to be due to a low volume fraction of α' phase (about 0.1%). The presence of a small fraction of α' phase can not be ruled out in the specimens implanted at 250 °C. In order to check this point, it is planned to perform Tomographic Atom Probe measurements using the implanted samples. However the presence of α' phase with a volume fraction of 0.1% would only affect to a very limited extent the results of the SANS analysis mentioned above.

4. Discussion

As mentioned in the introduction, implantation at 250 °C with 0.5 at.% helium induced a very large hardening of both EM10 and T91 specimens together with a total loss of ductility and an intergranular fracture mode, while following implantation at 550 °C hardening and embrittlement were much less severe [1]. In the following, we will discuss the possible causes for these modifications of the tensile properties, based on the present microstructural investigations performed using TEM and SANS. We will focus on the tensile properties measured following implantation at 250 °C. To our knowledge, a fully brittle intergranular fracture mode has never been reported before for conventional 9Cr martensitic steels tensile tested at room temperature.

The implantation process creates displacement damage, which amounts to approximately 0.8 dpa in the EM10 and T91 steels implanted to 0.5 at.% He (cf Section 2.1). To what extent does implantation-induced displacement damage contribute to the measured hardening? In order to address this question, we have plotted in Fig. 10 the change in yield stress of EM10 and T91 steels implanted to 0.5 at.% He or neutron irradiated at low temperature in various mixed-spectrum reactors as a function of displacement damage. In the latter case, the He production rate is very low (a few appm/dpa at most). Of course, since microstructural evolution and hence hardening of metallic materials depend on the irradiation temperature, it would have been preferable to plot data pertaining to steels irradiated at 250 °C, had they been available. We want to point out, however, that one data point (T91 irradiated in the Japanese reactor JMTR [11]) corresponds to a nominal irradiation temperature virtually equal to the implantation temperature. Moreover, even though the other two irradiation temperatures are either slightly lower or higher than 250 °C, all data points corresponding to neutron irradiated specimens seem to follow a common trend.

In addition to experimental results, we have also plotted in Fig. 10 the change in yield strength associated with the point defect clusters (black dot damage) detected by TEM in the EM10 and T91 specimens

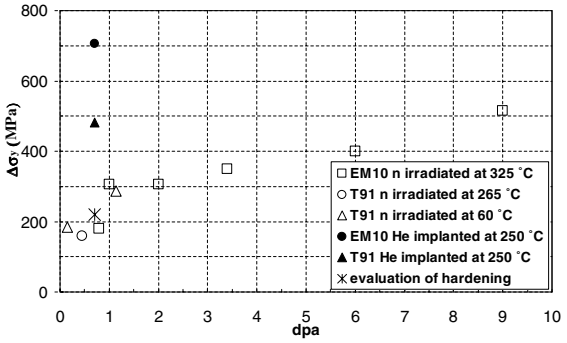

Fig. 10. Evolution of the yield stress increase as a function of displacement damage. The closed symbols refer to the EM10 and T91 specimens implanted to 0.5 at.% He at 250 °C [1]. The open symbols refer to specimens irradiated in different mixed-spectrum reactors. Circle: T91 specimen irradiated in JMTR [11], Triangles: T91 specimens irradiated in HFIR [12]. Squares: EM10 samples irradiated in OSIRIS [13,14]. Note that all materials were in the standard tempered conditions before implantation/irradiation. Star: evaluation of hardening based on TEM microstructural data (see text for detailed explanations).

implanted at 250 °C. The value of the yield stress increase $\Delta\sigma_y$ was calculated in accordance with the standard dispersed barrier hardening model (see for instance [15,16]) using Eq. (10):

$$\Delta\sigma_y = M\alpha\mu b(Nd)^{1/2}, \tag{10}$$

where μ is the shear modulus of the steel, b is the Burgers vector of the moving dislocation, α is the obstacle strength of small defect clusters, M is the averaged Taylor factor for a bcc polycristal in tension ($M \approx 3$ [17]), N is the number density of the obstacles and d their average diameter. We have assumed the following values for the different parameters: $\mu = 8 \times 10^4$ MPa, $\alpha = 0.4$, $b = 0.2$ nm, $N = 3.5 \times 10^{22}$ m^{-3} and $d = 3.7$ nm. The value for N and d were obtained by the TEM analysis (Section 3.1.2). The calculated value ($\Delta\sigma_y \approx 220$ MPa) follows the data trend for the change in yield strength as a function of irradiation dose rather well. However, it is obvious that the data points corresponding to the implanted samples are far above the trend. The main conclusion that can be drawn from this analysis, is that displacement induced microstructure (i.e. point defect clusters) cannot be the main cause of the very high degree of hardening displayed by the martensitic steels implanted at 250 °C to 0.5 at.% He.

Hunn et al. [18] came to the same conclusion (i.e. that hardening in He implanted steel specimens cannot be explained by displacement damage alone), based on nanohardness measurements performed on type 316 LN austenitic stainless steel specimens irradiated at 200 °C with either 360 keV He or 3.5 MeV Fe ions. These authors found that He-induced hardening increases far more rapidly as a function of irradiation dose than is the case for the specimens irradiated with Fe ions. This behaviour however was observed only above a threshold concentration equal to approximately 1 at.% He. The additional hardening in the He implanted specimens was attributed to the presence of a high number density of small He bubbles. Indeed bubble-like features could be detected by TEM above 1 at.% He and were clearly imaged above 5 at.%.

In the present case, the helium bubbles detected by SANS are also the most likely origin of the implantation-induced hardening. Eq. (10) with as input values the mean bubble diameter and number density obtained for EM10 implanted at 250 °C (Table 3) yields $\Delta\sigma_y \approx 870$ MPa. This value is of the right order of magnitude although somewhat larger than the measured hardening for EM10. However it must be pointed out that the tensile samples implanted at 250 °C and tested at room temperature broke before yield as clearly shown by the tensile curves and the SEM observations of the fractured specimens [1]. The T91 specimen broke in the elastic part of the test at a lower stress than the EM10 specimen. The values plotted in Fig. 10 are not increases in yield stress but rather the difference between the tensile strength of the implanted specimens, which did not reach yield point, and the yield stress of the virgin specimens. Hence it is not surprising that the estimated yield stress increase is larger than the values plotted in Fig. 10. One should also add that the values for bubble sizes and number densities which result from the SANS analysis might be somewhat overestimated as discussed in Section 3.2. In any case, the above evaluation confirms that helium bubbles are the main cause for the dramatic hardening displayed by the EM10 and T91 samples implanted at 250 °C to 5000 appm.

This concentration is half the threshold value above which, as mentioned above, a specific He induced hardening was measured by Hunn et al. A probable reason for this apparent discrepancy is not related to the different steels used in both studies, but rather to different implantation conditions. The implantation temperature was slighted lower in the experiments performed by Hunn et al. (200 °C) and the He injection rate (2 at ppm/s) was 2 orders of magnitude higher than that used in our experiments. Due to its extremely low solubility, He tends to form clusters when introduced into metallic materials. For a given He content and implantation temperature, He clusters will decrease in size and increase in number density as the injection rate increases. It may well be that He clusters formed during implantation at 2 at ppm/s to 0.5 at.% are too small to impede significantly dislocation motion whereas larger He bubbles such as those detected by SANS, are stronger obstacles to dislocation glide.

Ullmaier and Camus [2] performed tensile tests on He-implanted Manet (a 11% Cr martensitic steel) and 316L austenitic steel specimens. Experimental conditions (injection rate, total He content) were identical to those used in the experiments described here. However the implantation temperature was lower (between room temperature and 70 °C). Based on the comparison with other data on Manet steel irradiated in different radiation environments, the authors came to the conclusion that the observed increase in yield stress following implantation was due to displacement induced defects. The fact that helium did not contribute significantly to hardening was attributed to a fine dispersion in clusters containing only a few He atoms. This hypothesis is consistent with the microstructural information obtained at 250 °C by SANS since a decrease in implantation temperature from 250 to 70 °C, all other parameters being constant, will lead to a decrease in He cluster sizes.

It must be stressed that in contrast to what was observed on the specimens implanted at 250 °C [1], all Manet and 316L specimens implanted by Ullmaier and Camus at low temperature and tested at room temperature and at 300 °C displayed fully ductile and transgranular fracture surfaces. Is this difference in fracture behaviour mainly related to a higher implantation-induced hardening in the specimens implanted at 250 °C? While this is certainly an important contributing factor, we believe that this higher hardening is not the only explanation. In the following, we present experimental evidence to support this assumption.

Fig. 11 shows the evolution of the yield stress as a function of dose for EM10 samples irradiated at 325 °C in the experimental Osiris reactor [13,14] or implanted to 0.5 at.% He at 250 °C, respectively. The same EM10 heat (chemical composition is given in Table 1) was used in both experiments. However, thermal treatment prior to implantation or neutron irradiation was not the same. The implanted sample was in the standard metallurgical condition (i.e. tempered martensite) whereas the neutron-irradiated specimens were in the as-quenched metallurgical condition. It can be seen that neutron irradiation at 325 °C induced a large increase in yield stress, which reached at 6 dpa a value much higher than that measured in the case of the implanted sample. However, the specimen tested at RT following 6 dpa of exposure, still displayed significant ductility, as shown by the values of reduction of area, total elongation and uniform elongation equal to 56%, 9% and 1.2%, respectively. While fracture surface observations have not yet been performed on the specimen irradiated to 6 dpa and tested at RT, the fracture surface appearance of the tensile sample irradiated to 3.4 dpa and tested at 325 °C, whose yield stress is comparable to that of the implanted specimen, was found to be fully ductile as shown on Fig. 12.

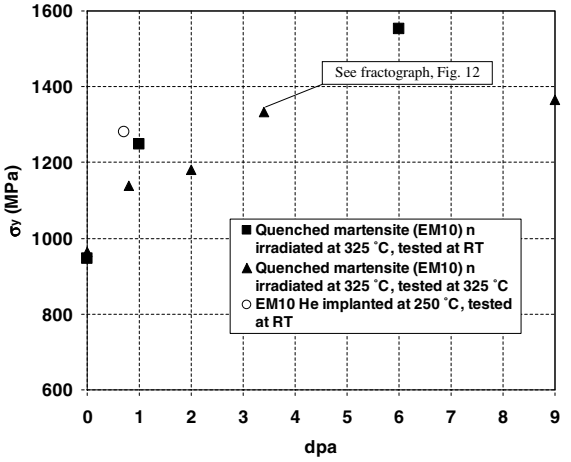

Fig. 11. Evolution of the yield stress as a function of irradiation dose for EM10 samples implanted at 250 °C or neutron irradiated in OSIRIS at 325 °C [13,14], respectively. See text for comments concerning the metallurgical conditions of the different specimens.

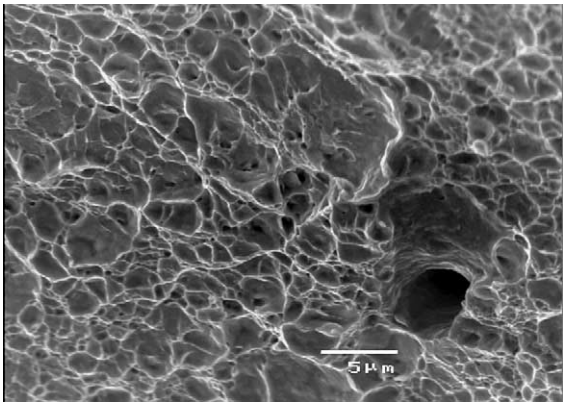

Fig. 12. EM10 specimen in the as-quenched metallurgical condition, irradiated to 3.4 dpa at 325 °C in OSIRIS and tested at 325 °C [13,14]. SEM micrograph showing the transgranular ductile failure mode.

Electronic structure calculations were recently performed by Gupta [19] in order to assess the effect of He when present in iron grain boundaries. It was shown that helium induces a large reduction in grain boundary cohesion. A similar prediction was made by Smith et al. [20] concerning the embrittling effect of He on nickel grain boundaries.

Therefore, it is suggested that both the high hardening of the grains following implantation at 250 °C and grain boundary weakening due to helium are the two main factors leading to the observed intergranular fracture mode. The high stress values reached during the tensile tests may be sufficient to induce crack nucleation

in the weakened PAG boundaries. This assumption is consistent with the fact that, for both EM10 and T91 samples implanted at 250 °C and tested at RT, fracture occurred in the fillet, i.e. in the region where stress concentration occurs under elastic deformation of the samples. Once nucleated, the crack propagates easily along the paths provided by the embrittled PAG boundaries. The presence of a high carbide density on the PAG boundaries may also promote crack nucleation and aid in the propagation of intergranular cracks, as suggested in the case of the so-called 'tempered martensite embrittlement' phenomenon (see for instance [21]).

5. Summary and conclusions

TEM and SANS were used to characterise the microstructures of EM10 and T91 martensitic steel samples implanted with 0.5 at.% helium at 250 and 550 °C, respectively. This microstructural analysis revealed the presence of small defect clusters in the steels implanted at 250 °C, as well as helium bubbles following implantation at both temperatures. Furthermore, the SANS experiments showed that these bubbles are close to thermodynamic equilibrium, i.e. their internal gas pressure is balanced by the surface tension.

The TEM study was performed on discs punched out from tensile specimens following the tests, which indicated for the samples implanted at 250 °C a very large hardening and a total loss of ductility associated with a predominantly intergranular fracture mode [1].

It was shown that the observed hardening is not due to the small defect clusters but to the high density of small He bubbles detected by the microstructural analysis. It is furthermore suggested that the brittle, intergranular fracture mode results from the combination of pronounced hardening and weakening of PAG boundaries due to helium.

A typical spallation environment is characterised by a lower He creation rate and a higher damage creation rate than in the case of the simulation experiments mentioned above. It is therefore expected that the helium distribution in the steels implanted at 250 °C be representative of that obtained after exposure in a spallation radiation field at lower temperature. Consequently, the severe embrittlement observed after implantation at 250 °C raises the question of the suitability of martensitic steels as structural materials for the ESS container window, which will operate below 250 °C. The results obtained in the present study do not, however, rule out the use of 9Cr martensitic steels for the Megapie or ADS proton beam windows since in both cases the operating temperature will be significantly higher than 250 °C. Nevertheless, additional data, both from simulation experiments and irradiation tests in a spallation spectrum, are obviously needed.

Appendix A. Intensity scattered by a population of small dislocation loops

The intensity scattered by a population of small dislocation loops of radius r with an isotropic distribution of orientations is given by [8]

$$\frac{1}{V_s}\mathrm{d}\Sigma/\mathrm{d}\Omega = \delta(b_{\mathrm{nuc}}^{\mathrm{m}}/\Omega_{\mathrm{m}})^2(1-2v)^2/(1-v)^2 4\pi^2(br/q)^2 \times \int_0^{\pi/2} \sin^3\theta J_1^2(qr\sin\theta)\,\mathrm{d}\theta, \quad (A.1)$$

where δ is the bubble number density, b the Burgers vector, v Poisson's ratio and J_1 the first-order Bessel function.

At small angles, an approximate expression for (A.1) is [8]:

$$\frac{1}{V_s}\mathrm{d}\Sigma/\mathrm{d}\Omega = I_0 \exp\left(-\frac{3}{14}q^2r^2\right), \quad (A.2)$$

$$\text{where} \quad I_0 = \delta(b_{\mathrm{nuc}}^{\mathrm{m}}/\Omega_{\mathrm{m}})^2 \frac{8\pi^2(1-2v)^2}{15(1-v)^2} b^2 r^4. \quad (A.3)$$

I_0 can be evaluated using the black-dot densities and mean sizes determined experimentally by TEM. For $\delta = 3.5\times10^{22}/\mathrm{m}^3$, $r = 2$ nm and $b = 0.2$ nm, one finds $I_0 = 9.2\times10^{-5}\ \mathrm{cm}^{-1}$. This value is more than 3 orders of magnitude smaller than intensity scattered by the specimens implanted at 250 °C over the whole investigated q-range. We therefore conclude that the black-dots do not contribute significantly to the scattered intensity.

References

[1] P. Jung, J. Henry, J. Chen, J.-C. Brachet, these Proceedings. doi:10.1016/S0022-3115(03)00014-X.
[2] H. Ullmaier, E. Camus, J. Nucl. Mater. 251 (1997) 262.
[3] J.P. Biersack, L.G. Haggmark, Nucl. Instrum. and Meth. 174 (1980) 93.
[4] J.F. Ziegler, Manual of TRIM Version 95.4, March 1995, unpublished.
[5] S.M. Allen, Philos. Mag. A 43 (1981) 325.
[6] J.P. Cotton, in: P. Lidner, Th. Zemb (Eds.), Neutron, X-Ray and Light Scattering, Elsevier, Amsterdam, 1991, p. 19.
[7] M.L. Jenkins, J. Nucl. Mater. 216 (1994) 124.
[8] A. Seeger, M. Rülhe, Ann. Physik 11 (1963) 216.
[9] Qiang-Li, W. Kesternich, H. Schroeder, D. Schwahn, H. Ullmaier, Acta Metall. Mater. 38 (1990) 2383.
[10] H. Trinkaus, Radiat. Eff. 78 (1983) 189.
[11] F. Abe, M. Narui, H. Kayano, Mater. Trans., JIM 34 (1993) 1053.
[12] K. Farrell, T.S. Byun, J. Nucl. Mater. 296 (2001) 129.
[13] J.C. Brachet, X. Averty, P. Lamagnère, A. Alamo, F. Rosenblum, O. Raquet, J.L. Bertin, in: S.T. Rosinski, M.L. Grossbeck, T.R. Allen, A.S. Kumar (Eds.), Effects of Radiation on Materials: 20th International Symposium,

ASTM STP 1405, ASTM, West Conshohocken, PA , 2001, 500520.
[14] X. Averty, J.P. Pizzanelli, O. Rabouille, J.J. Espinas, J.C. Brachet, in press.
[15] A.J. Ardell, Met. Trans. A 16 (1985) 2131.
[16] G.E. Lucas, J. Nucl. Mater. 206 (1993) 287.
[17] U.F. Kocks, Met. Trans. 1 (1970) 1121.
[18] J.D. Hunn, E.H. Lee, T.S. Byun, L.K. Mansur, J. Nucl. Mater. 282 (2000) 131.
[19] R. Gupta (CEA-SRMP), in press.
[20] R.W. Smith, W.T. Geng, C.B. Geller, R. Wu, A.J. Freeman, Scr. Mater. 43 (2000) 957.
[21] C.L. Briant, Mater. Sci. Technol. 5 (1989) 138.
[22] Aldred, Phys. Rev. B 14 (1976) 219.
[23] N.W. Ashcroft, J. Lekner, Phys. Rev. 145 (1966) 83.
[24] M.H. Mathon, Y. de Carlan, G. Geoffroy, X. Averty, A. Alamo, C.H. de Novion, J. Nucl. Mater. 312 (2003) 236.